

Tuning the structural, optical, photoluminescence and dielectric properties of Eu^{2+} -activated mixed strontium aluminate phosphors with different rare earth co-activators

M. M. S. Sanad^{1,2} · M. M. Rashad¹

Received: 19 February 2016 / Accepted: 2 May 2016 / Published online: 6 May 2016
© Springer Science+Business Media New York 2016

Abstract Different phosphor colors of SrAl_xO_y : $\text{Eu}_{0.01}^{2+}$, $\text{R}_{0.01}^{3+}$ ($\text{R} = \text{Er}^{3+}$, Tm^{3+} and Tb^{3+}) nanopowders and pellets have been synthesized via citrate combustion technique. XRD results revealed that monoclinic SrAl_2O_4 was the major phase and hexagonal $\text{SrAl}_{12}\text{O}_{19}$ was the minor phase. Meanwhile, Field emission SEM images showed hollow cylindrical-like shape structures filled with the large number of nanorods for the SrAl_xO_y : $\text{Eu}_{0.01}^{2+}$, $\text{Tb}_{0.01}^{3+}$ sample. The values of measured band gap energy and calculated refractive index were mainly dependant on the ionic radius of R^{3+} co-doping ion. The PL emission spectra and afterglow properties were strongly affected by the lanthanide type (R^{3+}). For instance, Eu^{2+} - SrAl_xO_y sample achieved the maximum dielectric permittivity (ϵ') ~ 16.77 and dielectric loss ($\tan\delta$) ~ 0.19 at the *microwave* frequency region (1 GHz). Meanwhile, Tb^{3+} , Eu^{2+} - SrAl_xO_y sample was possessed the minimum dielectric permittivity (ϵ') ~ 1.36 and dielectric loss ($\tan\delta$) ~ 0.0002 at the *radiowave* frequency region (100 MHz).

1 Introduction

Eu^{2+} -activated strontium aluminate phosphors have shown a great potential for various applications such as luminous paints, emergency signs, photo-sensitizers, biological

probes and medical diagnostics [1–5]. Particularly, Eu^{2+} , Dy^{3+} -codoped strontium aluminate material have attracted much interest because of their excellent properties such as non-toxicity, chemical stability, high quantum efficiency and long afterglow brightness (i.e. phosphorescence) in comparison with sulfide based luminescent materials [6–10]. In context, it is known that the activator is acting as a luminescence center which allows the 4f-5d transitions from the low energy levels in the host. Meanwhile, the co-activator (i.e. co-dopant) is thought to produce very bright and long-lasting phosphorescence at room temperature because of the creation of highly dense hole trapping levels at the optimal depth [11]. In this regard, most of the published papers during the last few years have focused on studying the effect of different activators such as Eu^{2+} , Pr^{3+} , Tb^{3+} , Ce^{3+} and Sm^{2+} , ... etc. on the luminescence emission properties of strontium aluminate host materials [12–16]. Furthermore, a plenty of preparation methods have been reported for synthesis of the long persistent Eu^{2+} , Dy^{3+} -codoped strontium aluminate phosphors of different crystalline forms including SrAl_2O_4 , $\text{Sr}_4\text{Al}_2\text{O}_7$, $\text{Sr}_3\text{Al}_2\text{O}_6$, $\text{SrAl}_{12}\text{O}_{19}$, $\text{Sr}_4\text{Al}_{14}\text{O}_{25}$ [17–21]. Otherwise, there is a significant lack in the research studies concerning the effect of co-dopant (i.e. co-activator) ions rather than Dy^{3+} ion which are mainly responsible for the afterglow phenomena of all photoluminescence materials. Moreover, only one published article has been found to study the photoluminescence effect of Yb^{3+} as co-dopant with Eu^{2+} - SrAl_2O_4 [22]. To the best of our knowledge, the effects of lanthanide cations (Er^{3+} , Tm^{3+} and Tb^{3+}) as co-dopant with Eu^{2+} - SrAl_xO_y on photoluminescence, afterglow properties have not been systematically investigated before. Accordingly, the present work aims at synthesis of Eu^{2+} - SrAl_xO_y and R^{3+} , Eu^{2+} - SrAl_xO_y nano-structured powders via a facile citrate combustion method. Moreover,

✉ M. M. S. Sanad
mustafa_sanad2002@yahoo.com

¹ Central Metallurgical R&D Institute (CMRDI),
P.O. Box 87, Helwan, Cairo, Egypt

² Laboratory of Electrochemistry and Physicochemistry of
Materials and Interfaces, Institut polytechnique de Grenoble,
BP 75, 38402 St Martin d'Hères Cedex, France

the structural, optical, photoluminescence and afterglow properties of the as-prepared phosphors will sufficiently be studied. Furthermore, the dielectric performance of phosphors ceramic samples will actually be evaluated in terms of the changes in dielectric permittivity, dissipation and quality factors.

2 Experimental

2.1 Materials and methods

Anhydrous strontium nitrate $\text{Sr}(\text{NO}_3)_2$ (Sigma-Aldrich 99.9 %), $\text{Al}(\text{NO}_3)_3 \cdot 9\text{H}_2\text{O}$ (Sigma-Aldrich 99.9 %), europium nitrate hexahydrate $\text{Eu}(\text{NO}_3)_3 \cdot 6\text{H}_2\text{O}$ (Alfa Aesar 99.9 %), erbium acetate tetrahydrate $\text{Er}(\text{OAc})_3 \cdot 4\text{H}_2\text{O}$ (Alfa Aesar 99.9 %), thulium acetate hydrate $\text{Tm}(\text{OAc})_3 \cdot x\text{H}_2\text{O}$ (Sigma-Aldrich 99.9 %), terbium nitrate pentahydrate $\text{Tb}(\text{NO}_3)_3 \cdot 5\text{H}_2\text{O}$ (Sigma-Aldrich 99.9 %) and citric acid $\text{C}_6\text{H}_8\text{O}_7$ (Sigma-Aldrich 99.5 %) were employed as raw materials. Deionized water was used in the whole work.

Strontium aluminate phosphors of chemical composition SrAl_xO_y : $\text{Eu}_{0.01}^{2+}$ ($x = 3.5$) and SrAl_xO_y : $\text{Eu}_{0.01}^{2+}$, $\text{R}_{0.01}^{3+}$ (Er^{3+} , Tm^{3+} or Tb^{3+}) nanorods were synthesized via a citrate combustion method. In typical synthesis, salts of Sr, Al and Eu (1 wt%) were dissolved in 0.5 M citric acid solution which act as a fuel and a complexing agent. Then, about 1 wt% of R^{3+} (Er^{3+} , Tm^{3+} or Tb^{3+}) salts was also added for precursor preparation of the codoped strontium aluminate phosphors SrAl_xO_y : Eu^{2+} , R^{3+} . After that, the mixed solutions were then boiled to evaporate the excess water. Thereafter, the resulting viscous liquid started to undergo auto-combustion after putting the glass beaker directly in a muffle furnace (at 400 °C) yielding grayish dark fluffy precursor powders. Finally, the obtained combustion precursors were pre-calcined at 1000 °C for 6 h in an air atmosphere to remove the residual carbon. Thereafter, these powders were calcined again at 1300 °C for 3 h with heating rate (5°min^{-1}) in presence of gas mixture (argon 95 % and hydrogen 5 %). The reducing H_2 gas of 5 % was injected in order to ensure complete conversion of activator ion Eu^{3+} into Eu^{2+} ion. Pellets of these phosphors were prepared by pressing the ground powders in a 12 mm diameter steel die at a pressure of 50 MPa followed by sintering at 1400 °C for 5 h at the same heating and reducing conditions.

2.2 Sample characterization

X-ray powder diffraction (XRD) was carried out on a model Bruker AXS diffractometer (D8-ADVANCE Germany) with Cu $\text{K}\alpha$ ($\lambda = 1.54056 \text{ \AA}$) radiation, operating at 40 kV and 40 mA. The diffraction data were recorded for

2θ values between 10° and 60° and the scanning rate was 3°min^{-1} or $0.02^\circ/0.4 \text{ s}$. The particle morphology was inspected by a field emission scanning electron microscopy FE-SEM (JEOL-JSM-5410 Japan). The optical measurements were implemented using UV–Vis–NIR scanning spectrophotometer (Perkin Elmer Lambda 1050 Spectrophotometer, USA) using 1 cm path length quartz cell. Photoluminescence (PL) spectra were obtained at room temperature using fluorescence spectrophotometer (SHIMADZU RF-5301PC Japan) with xenon discharge lamp (150 W) as excitation source. Handheld ultraviolet lamp long wavelength (365 nm UVA) was also used to inspect the afterglow characteristics of the prepared phosphors. Dielectric properties of sintered pellets were measured using a network impedance analyzer (Agilent-E4991A, USA) that is responsible for generation and reception of a signal in the frequency range of 1 MHz–3 GHz.

3 Results and discussion

3.1 Crystal structure

Figure 1 shows the effect of co-doped R^{3+} ions (Er^{3+} , Tm^{3+} or Tb^{3+}) on the phase composition of Eu^{2+} -activated strontium aluminate powders post-annealed at 1300 °C for 3 h with constant concentration of R^{3+} (1 %). The XRD results indicate that the evolution of two main phases, SrAl_2O_4 (major phase) of solid lines and $\text{SrAl}_{12}\text{O}_{19}$ (minor phase) of dotted lines as illustrated in Fig. 1. The diffraction peaks of α - SrAl_2O_4 phase matched very well with

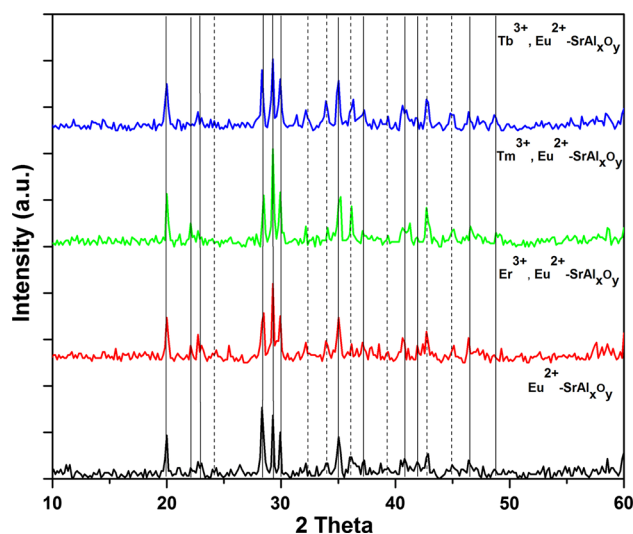


Fig. 1 XRD patterns of Eu^{2+} -doped and R^{3+} , Eu^{2+} -doped SrAl_xO_y powders, *solid lines* indicate SrAl_2O_4 (JCPDS: 74-0794), *dotted lines* indicate $\text{SrAl}_{12}\text{O}_{19}$ (JCPDS: 80-1195)

JCPDS card no. 74-0794 indicating the formation of monoclinic crystal structure with space group $P2_1$ [23]. It is needle to note that the formed SrAl_2O_4 phase exists in the most stable phase (α - SrAl_2O_4) and cannot be converted into the undesired β -form due to the high temperature preparation conditions [24]. Meanwhile, the other diffraction peaks of $\text{SrAl}_{12}\text{O}_{19}$ are found to be matched perfectly with JCPDS card no. 80-1195 of hexagonal structure and space group $P63/mmc$ [25]. In addition, it is found that the intensities of the main diffraction peaks for $\text{SrAl}_{12}\text{O}_{19}$ phase are clearly increased in case of Tm^{3+} or Tb^{3+} doping, which demonstrates the enhancing of the crystallinity degree and good distribution for the mixed phases. Evidently, no obvious impurity phases such as β - SrAl_2O_4 , $\text{Sr}_3\text{Al}_2\text{O}_6$ and $\text{Sr}_4\text{Al}_{14}\text{O}_{25}$ can be detected. Furthermore, the most diffraction peaks are very broad, indicating a small crystal size.

3.2 Crystal morphology

Figure 2a, c displays the typical FE-SEM images of SrAl_xO_y : $\text{Eu}_{0.01}^{2+}$ and SrAl_xO_y : $\text{Eu}_{0.01}^{2+}$, $\text{Tb}_{0.01}^{3+}$ annealed at 1300 °C for 3 h under reducing atmosphere. It clearly crystallized in hollow cylindrical-like shape structures. The outer surface of these hollow tubes consists of connected, uniform and smooth crystalline spherical particles with the relative average particle diameter (500–200) nm. The inner surface of these hollow tubes demonstrates a large number of nanorods of average length (200–300) nm and average width (20–50) nm as represented in the magnified views Fig. 2b, d. However, the numbers of the nanorods evolved inside this hollow structure are significantly increased in case of co-doping of strontium aluminate with both Eu^{2+} and Tb^{3+} ions. This could be attributed to the interactive effects of multiple dopants which evidently induce the nanorods growth dynamics creating an intrinsically anisotropic structure [26–29].

3.3 Optical properties

3.3.1 Band gap energy

The optical properties of all synthesized strontium aluminate phosphors are examined by UV–Vis–NIR spectrophotometer using integrating sphere unit and the obtained band gap energy results are listed in Table 1. The transmittance spectrum measurements of all phosphors have been accomplished in the wavelength range 250–800 nm at room temperature as shown in Fig. 3A. Mainly, the transmission spectra are occurred between wavelength range 275 and 375 nm for these samples.

The optical absorbance A and the optical absorption coefficient “ α ” have been obtained using the following relations [30, 31]:

$$\text{Log}(1/T) = \alpha t \quad (1)$$

$$\text{The absorbance } A = \text{Log}(I^\circ/I) = \alpha t \quad (2)$$

$$\text{Transmittance } \%T = 100(I^\circ/I) \quad (3)$$

where T is the transmittance of the spectra, t is the thickness of samples cell, I° and I are the intensities of the incident and passed light through the sample.

Analysis of optical absorption spectra is one of the most productive tools for determining optical band gap of the film. Therefore, the band gap energy was determined by extrapolating the absorption coefficient (α) to zero from the spectral data (Fig. 4).

The absorption coefficient was calculated by the following equation

$$(\alpha h\nu)^m = h\nu - E_g \quad (4)$$

where α is the absorption coefficient, $h\nu$ is the photon energy, E_g is the band gap energy, $m = 1/2$ or $3/2$ for indirect allowed and indirect forbidden transitions, and $m = 2$ or 3 for direct allowed and direct forbidden transitions. Evidently, band gaps are calculated by plotting $(\alpha h\nu)^2$ against $h\nu$ and extrapolating the linear portion of the curve on $h\nu$ axis to $\alpha = 0$ is shown in Fig. 5b. It is found that SrAl_xO_y : $\text{Eu}_{0.01}^{2+}$, $\text{Tb}_{0.01}^{3+}$ sample posses the lowest E_g value among those of other samples. For instance, it is also seen that the ionic radius of the rare earth dopants are in the following order ($\text{Tm}^{3+} < \text{Er}^{3+} < \text{Tb}^{3+} < \text{Eu}^{2+}$). Therefore, our band gap energy measurements are in good agreement with the fact of increasing E_g value with decreasing ionic radius of doping ion and vices versa [32–35].

3.3.2 Refractive index

The refractive index (n) of semiconducting materials is very important in determining the optical properties of the material. Knowledge of n is essential to design heterostructure lasers in optoelectronic devices as well as in solar cell applications.

The refractive index (n) of the samples can be calculated using Herve and Vandamme relation [36]. Where E_g is the energy band gap.

$$n = \sqrt{1 + \left(\frac{A}{E_g + B}\right)^2} \quad (5)$$

where, A and B are numerical constants with values of 13.6 and 3.4 eV, respectively. The calculated averages of the refractive index for Eu^{3+} -doped and R^{3+} , Eu^{3+} -doped

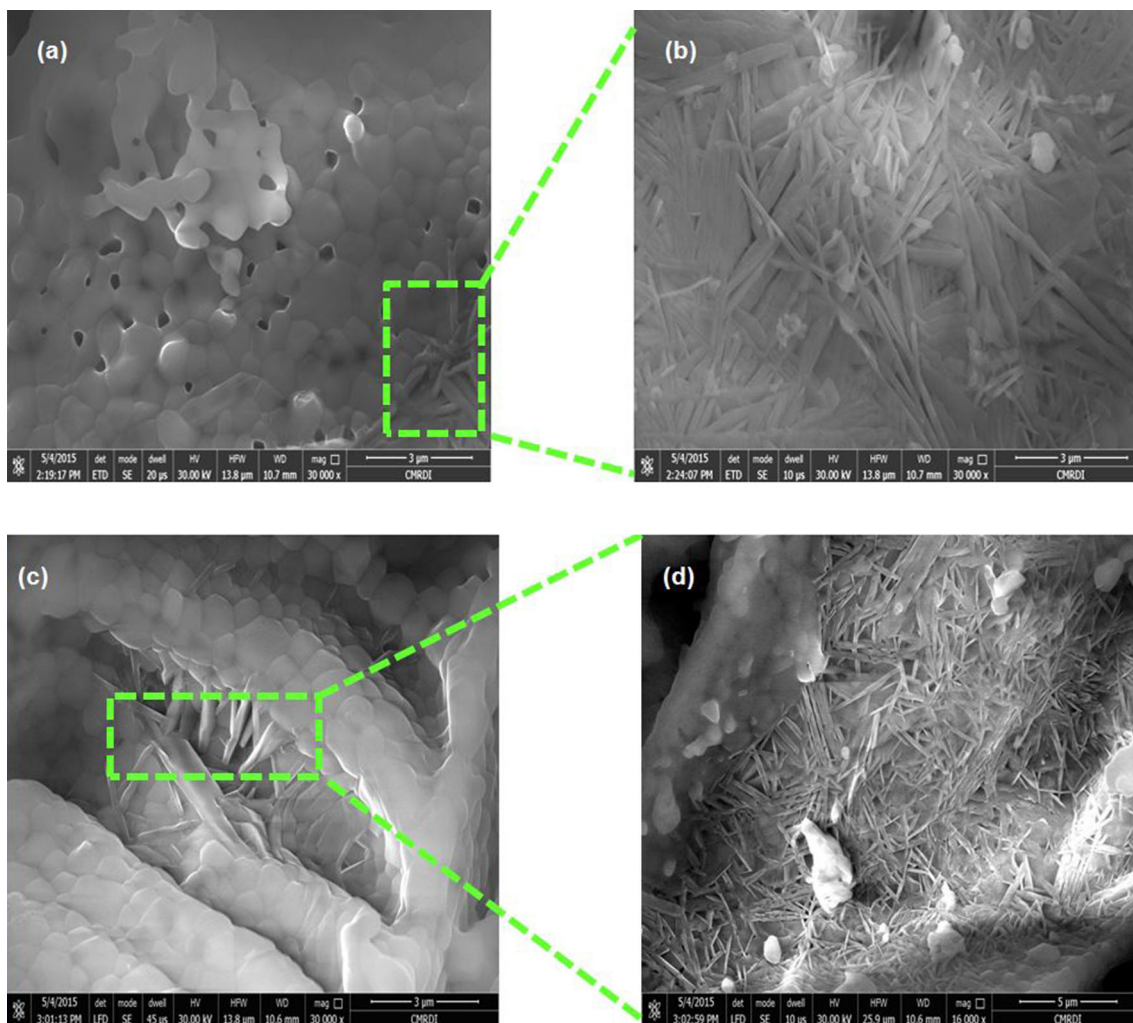


Fig. 2 FE-SEM images of Eu^{2+} -doped SrAl_xO_y powders (**a, b**) and Tb^{3+} , Eu^{2+} -doped SrAl_xO_y powders (**c, d**)

Table 1 Effect of R^{3+} cations on the optical properties of Eu^{2+} - SrAl_xO_y phosphor powders

Phosphor sample	E_g (eV)	Refractive index (n)	CIE Coordinates		Color of emitted light
			x	y	
Eu^{2+} - SrAl_xO_y	3.72	1.706	0.215	0.668	Lime green
Er^{3+} , Eu^{2+} - SrAl_xO_y	3.85	1.696	0.315	0.331	Warm white
Tm^{3+} , Eu^{2+} - SrAl_xO_y	3.75	1.704	0.118	0.611	Blue green
Tb^{3+} , Eu^{2+} - SrAl_xO_y	3.53	1.721	0.201	0.335	Light blue

samples are recorded in Table 1. Figure 3C shows the variation in the refractive indices against the band gap energies. It is indicated that the maximum refractive index (n) was 1.721 at 3.53 eV for SrAl_xO_y : $\text{Eu}_{0.01}^{2+}$, $\text{Tb}_{0.01}^{3+}$ sample. Moreover, it can also be implied that the refractive indices are shifted towards lower values at higher E_g values. Such obtained results confirmed that the change in the refractive indices is mainly dependent on the absorption features of these phosphors.

3.4 Photoluminescence (PL) and Afterglow (AG) properties

3.4.1 Photoluminescence (PL) spectroscopic analysis

Figure 5a–d reveals the typical PL emission spectrum of the as-prepared phosphors after excitation at different wavelengths (365, 380, 390 and 410 nm). The characteristic broad emission band of all phosphors is observed with

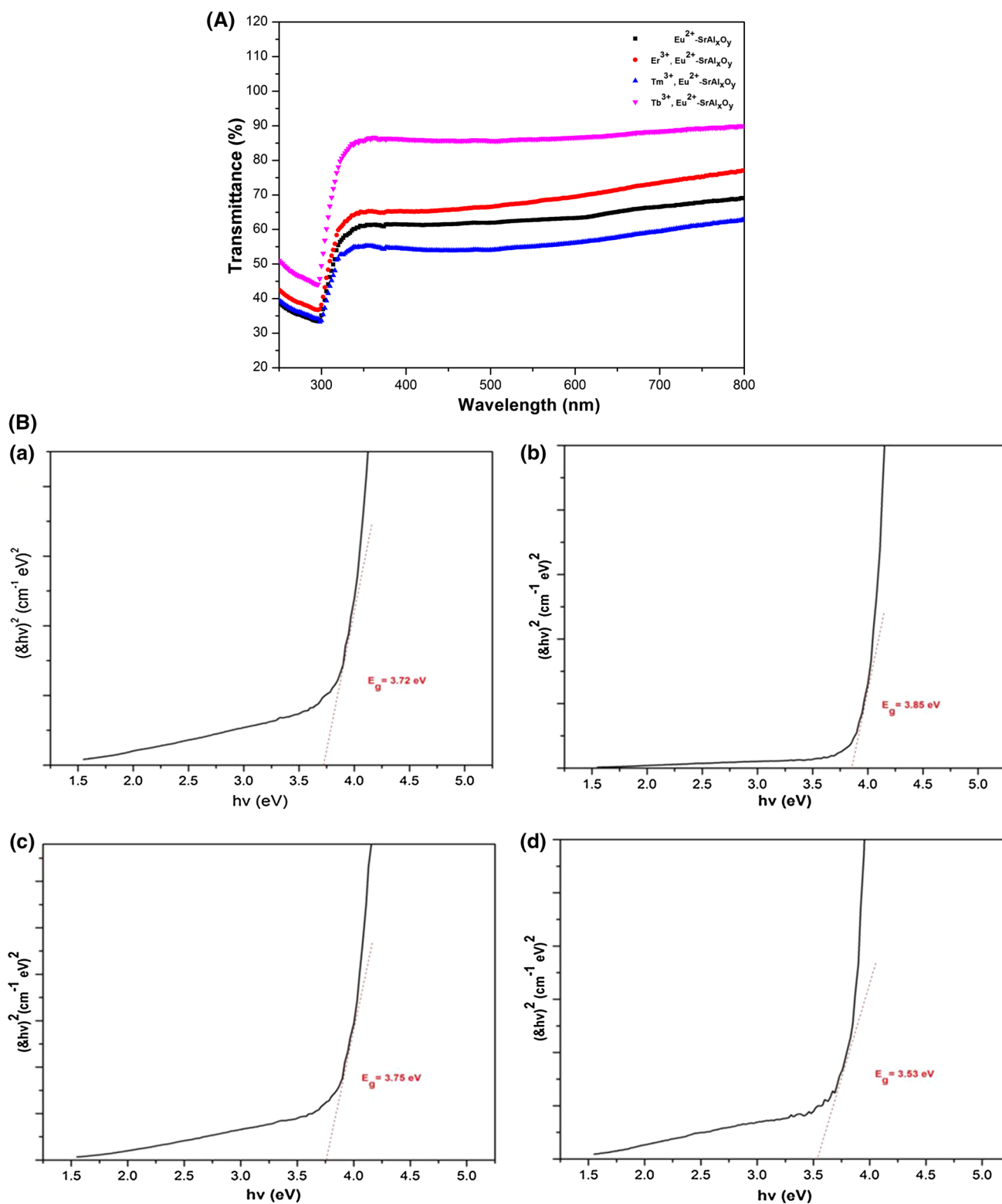


Fig. 3 **A** UV-Vis transmittance spectra of the as-synthesized phosphors. **B** Energy band gap of Eu^{2+} -doped SrAl_xO_y (**a**), Er^{3+} , Eu^{2+} -doped SrAl_xO_y (**b**), Tm^{3+} , Eu^{2+} -doped SrAl_xO_y (**c**) and Tb^{3+} , Eu^{2+} -

doped SrAl_xO_y powders (**d**). **C** Optical band gap energy versus the calculated refractive indices of phosphors powders

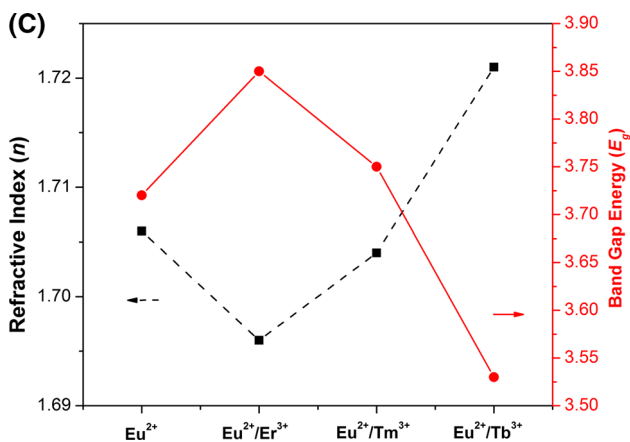


Fig. 3 continued

a peak collected at 513 nm, which coincided with previous published reports [22, 37–39]. In fact, the excitation transitions of Eu²⁺ centers 4f-4f5d occur immediately upon UV–Vis illumination, causing a large number of holes and electrons. Meanwhile, the created holes are transferred through the valence band and then trapped by the co-dopant ion R³⁺ (Er³⁺, Tm³⁺ or Tb³⁺) which thus turns into R⁴⁺. Furthermore, Eu²⁺ becomes an excited Eu⁺ after the capture of the excited electrons by the conduction band. After the termination of UV–Vis excitation, the hole is thermally released to the valence band again and migrates to the excited Eu⁺ ion where it is captured. As a result recombination takes place, i.e. the excited Eu⁺ returns to the Eu²⁺ ground state, which gives rise to the persistent luminescence properties [7, 40–42].

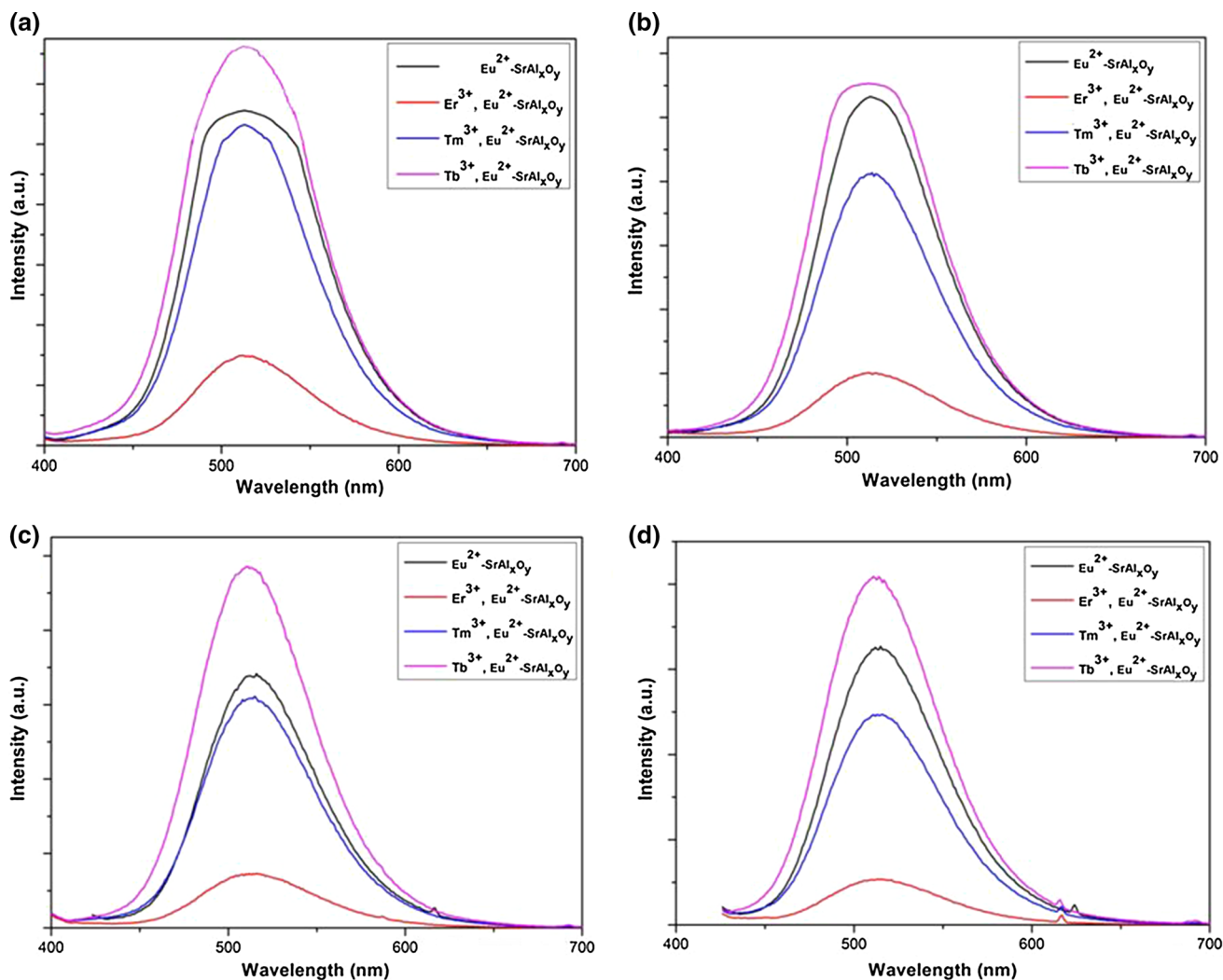


Fig. 4 PL emission spectra of all prepared phosphors at different excitation wavelengths **a** $\lambda_{\text{Excitation}} = 365$ nm, **b** $\lambda_{\text{Excitation}} = 380$ nm, **c** $\lambda_{\text{Excitation}} = 390$ nm, **d** $\lambda_{\text{Excitation}} = 410$ nm

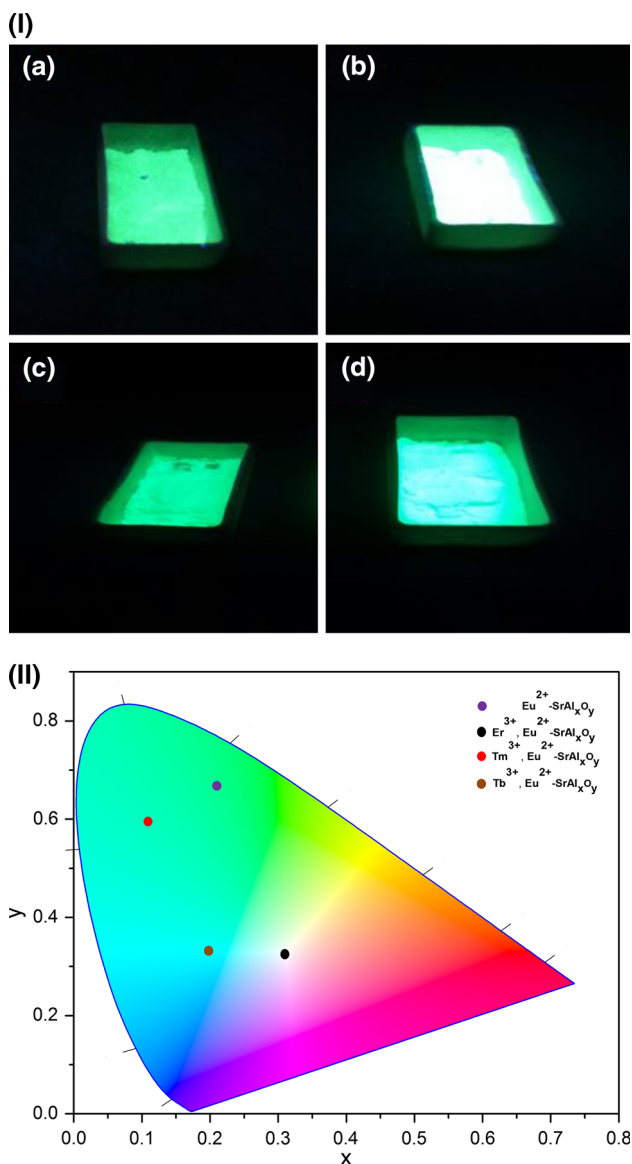


Fig. 5 I Afterglow characteristics for the excited phosphors after UV light irradiation of $\lambda = 365$ nm for 10 min. **a** $\text{Eu}^{2+}\text{-SrAl}_x\text{O}_y$, **b** $\text{Er}^{3+}\text{-SrAl}_x\text{O}_y$, **c** $\text{Tm}^{3+}\text{-SrAl}_x\text{O}_y$, **d** $\text{Tb}^{3+}\text{-SrAl}_x\text{O}_y$ powders. **II** CIE chromaticity diagram with color coordinate points of different strontium aluminate phosphors

Generally, the ion radius of R^{3+} (Er^{3+} , Tm^{3+} or Tb^{3+}) is smaller than that of Eu^{2+} (0.112 nm). Consequently, the solid solubility of R^{3+} in SrAl_xO_y is greater than that of Eu^{2+} . Therefore, this effect can lead to much more traps. However, it is seen that both the intensity and full width at half maximum (FWHM) of PL emission peaks of the co-doped phosphors are in the following order $\text{Tb}^{3+} > \text{Tm}^{3+} > \text{Er}^{3+}$, which can be explained by the value order of ionic radii difference between Eu^{2+} and R^{3+} ions according to the order $(\text{Eu}^{2+}\text{-Tb}^{3+}) < (\text{Eu}^{2+}\text{-Tm}^{3+}) < (\text{Eu}^{2+}\text{-Er}^{3+})$. Accordingly, the SrAl_xO_y : $\text{Eu}^{2+}_{0.01}$, $\text{Tb}^{3+}_{0.01}$ sample gave the highest PL emission intensity due to the

largest number of trapping and releasing effects easily happened with lowest value of ionic radii difference.

3.4.2 Afterglow characteristics

Figure 5I a–d shows the images of the phosphors, which are obtained in a dark room using a digital camera after exposed to 365 nm ultraviolet lamp for 10 min. It is clear that the $\text{Eu}^{2+}\text{-SrAl}_x\text{O}_y$ acquired a lime green color of emitted light. Besides, the co-doped samples depicted white, blue-green and light blue afterglow colors for Er^{3+} , $\text{Eu}^{2+}\text{-SrAl}_x\text{O}_y$, Tm^{3+} , $\text{Eu}^{2+}\text{-SrAl}_x\text{O}_y$ and Tb^{3+} , $\text{Eu}^{2+}\text{-SrAl}_x\text{O}_y$ samples, respectively. All these emissions can be verified by determining the color coordinates x and y . The CIE chromatic coordinates can be calculated by integration of the X , Y , and Z values [43]. Figure 5II illustrates the CIE chromaticity coordinates diagram for the same phosphors excited at 365 nm. The calculated chromaticity coordinates for lime green light emitted from $\text{Eu}^{2+}\text{-SrAl}_x\text{O}_y$ phosphor are ($x = 0.215$, $y = 0.668$). Moreover, the corresponding coordinates for white, blue-green and light blue emission colors are found to be ($x = 0.315$, $y = 0.331$), ($x = 0.118$, $y = 0.611$) and ($x = 0.201$, $y = 0.335$), respectively. The obtained results are found to be in a good match with recently measured values for strontium aluminate phosphors [14, 24, 44–46].

3.5 Dielectric properties

The dielectric behavior of all phosphor pellets will be systematically investigated by studying the most important parameters, including the dielectric permittivity (ϵ'), dielectric loss ($\tan\delta$) and quality factor (Qf) within the frequency range (10 MHz–1 GHz). Figure 6a represents the variations of real part of permittivity in the frequency range (10 MHz–1 GHz) for the strontium aluminate phosphors. Even though it was difficult to locate studies on the dielectric properties of strontium aluminate phosphors, we did find a few studies that included dielectric data for this kind of host materials. It is revealed that the values of dielectric permittivity are exponentially increased with increasing frequency from 10 to 1000 MHz (1 GHz). In particular, the dielectric permittivity (ϵ') value are found to be in the following order $\text{Eu}^{2+}\text{-SrAl}_x\text{O}_y > \text{Er}^{3+}$, $\text{Eu}^{2+}\text{-SrAl}_x\text{O}_y > \text{Tb}^{3+}$, $\text{Eu}^{2+}\text{-SrAl}_x\text{O}_y > \text{Tm}^{3+}$, $\text{Eu}^{2+}\text{-SrAl}_x\text{O}_y$. The reason for such shallow and common decrease in case of R^{3+} and Eu^{2+} co-doped samples is due to the production of oxygen ions vacancies and holes by R^{3+} co-doping ions more than that produced by Eu^{2+} , leading to a higher extent of ions mobility and electronic conductivity [47–49].

The inset graph, Fig. 6b, shows the variation of the dielectric loss at in the frequency range (10 MHz–1 GHz) for the strontium aluminate phosphors. Clearly, it can be

Fig. 6 a Dielectric permittivity for all prepared phosphors at frequency range (10.0 MHz–1.0 GHz), **b** *Inset graph* for dielectric loss at the same frequency range

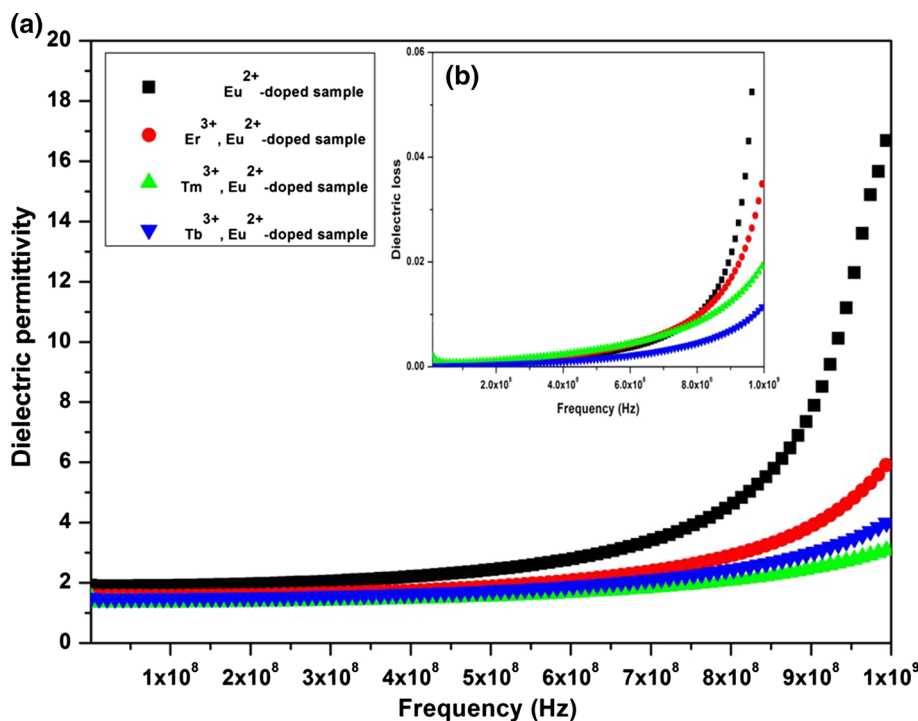


Table 2 Effect R^{3+} cations on the dielectric properties of Eu^{2+} - $SrAl_xO_y$ phosphor sintered pellets

Phosphor sample	Dielectric permittivity (ϵ')		Loss tangent ($\tan\delta$)		Quality factor (Qf)	
	At 100 MHz	At 1 GHz	At 100 MHz	At 1 GHz	At 100 MHz ($\times 10^4$)	At 1 GHz ($\times 10^4$)
Eu^{2+} - $SrAl_xO_y$	1.91	16.77	0.0004	0.1909	0.250	0.001
Er^{3+} , Eu^{2+} - $SrAl_xO_y$	1.56	6.06	0.0005	0.0374	0.172	0.003
Tm^{3+} , Eu^{2+} - $SrAl_xO_y$	1.49	3.15	0.0008	0.0199	0.123	0.005
Tb^{3+} , Eu^{2+} - $SrAl_xO_y$	1.36	4.09	0.0002	0.0119	0.500	0.008

seen that the dielectric loss ($\tan\delta$) value of R^{3+} , Eu^{2+} - $SrAl_xO_y$ samples are higher than Eu^{2+} - $SrAl_xO_y$ sample in the radiowave frequency region 10–100 MHz. This significant increase might be related to the formation of defects and ionic vacancies results in bonding of the co-doped material becoming more ionic in nature, thereby increases dielectric loss also [49, 50]. However, the values of dielectric loss for all phosphors samples were within the range (10^{-2} – 10^{-3}) which considered as an acceptable range for applying such ceramic materials in electronic packaging [51].

Since dielectric loss, dissipation factor or loss tangent ($\tan\delta$) is the ratio of the power loss in a dielectric material to the total power transmitted through the dielectric. Therefore, low dielectric loss is desirable for reducing heat generation at high frequency and high resistivity. Accordingly, the dielectric quality factor (Qf) is equivalent to the

reciprocal of the dielectric dissipation factor ($\tan\delta$). The values of (ϵ'), ($\tan\delta$) and (Qf) at two frequency regions 100 MHz and 1 GHz are summarized at Table 2. Obviously, Eu^{2+} - $SrAl_xO_y$ showed the highest dielectric permittivity (ϵ') ~ 16.77 and dielectric loss ($\tan\delta$) ~ 0.19 at the microwave frequency region (1 GHz). Moreover, it exhibited the lowest quality factor (Qf) ~ 10 at the microwave frequency region (1 GHz). On the other hand, Tb^{3+} , Eu^{2+} - $SrAl_xO_y$ possessed the lowest dielectric permittivity (ϵ') ~ 1.36 and dielectric loss ($\tan\delta$) ~ 0.0002 at the radiowave frequency region (100 MHz). Furthermore, it displayed the highest quality factor (Qf) ~ 5000 at the radiowave frequency region (100 MHz). Most of the obtained results from the dielectric measurements of strontium aluminate phosphors are in a good agreement with the few published results about the same kind of host materials [52–54].

4 Conclusion

SrAl_xO_y: Eu²⁺, R_{0.01}³⁺ nanopowders and pellets have been fabricated via citrate combustion technique. The changes in crystal structure and morphology of the formed particles have been investigated in presence and absence of lanthanide co-dopant ions (Er³⁺, Tm³⁺ or Tb³⁺). α-SrAl₂O₄ phase was the dominant phase with monoclinic crystal structure, while SrAl₁₂O₁₉ was the minor phase with hexagonal crystal structure. FE-SEM results confirmed the intrinsic anisotropic structure of nanorods for Tb³⁺, Eu²⁺-SrAl_xO_y hollow tube-like structure. However, Eu²⁺-SrAl_xO_y sample exhibited similar morphologies accompanied with few numbers of nanorods. The Er³⁺, Eu²⁺-SrAl_xO_y sample showed the maximum band gap energy ~3.85 eV, while Tb³⁺, Eu²⁺-SrAl_xO_y gave the minimum band gap energy ~3.53 eV. Photoluminescence emission intensity and FWHM of the co-doped phosphors were noticeably increased with decreasing ionic radii difference between activator (Eu²⁺) and co-activator (R³⁺). The values of dielectric permittivity (ϵ') and dielectric loss ($\tan\delta$) at low frequency ranges (MHz) were smaller than those at high frequency ranges (GHz) and vice versa for the values of quality factor (Q_f). Dielectric measurements of Tb³⁺, Eu²⁺-SrAl_xO_y sample showed a noticeable decrease in the dielectric permittivity by about 28.7 % region and strong increase in the quality factor by about 50 % in the *radio* frequency region.

References

- S.K. Zand, S. Baghshahi, M. Rajabi, J. Mater. Sci. Mater. Electron. **25**, 4412 (2014)
- D. Poelman, N. Avci, P.F. Smet, Opt. Exp. **17**, 358 (2009)
- H. Sun, L. Pan, G. Zhu, X. Piao, L. Zhang, Z. Sun, Dalton Trans. **43**, 14936 (2014)
- Q.L. Masne de Chermont, C. Chaneac, J. Seguin, F. Pelle, S. Maitrejean, J.P. Jolivet, D. Gourier, M. Bessodes, D. Scherman, Proc. Natl. Acad. Sci. USA **104**, 9266 (2007)
- S.K. Singh, RSC Adv. **4**, 58674 (2014)
- K. Pavani, J.S. Kumar, T. Sasikala, B.C. Jamalaih, H.J. Seo, L. Rama Moorthy, Mater. Chem. Phys. **129**, 292 (2011)
- T. Matsuzawa, Y. Aoki, N. Takeuchi, Y. Murayama, J. Electrochem. Soc. **143**, 2670 (1996)
- B.C. Cheng, H.J. Liu, M. Fang, Y.H. Xiao, S.J. Lei, L.D. Zhang, Chem. Commun. 944–946 (2009)
- H. Ping, C. Cai-E, W. Sen, Chin. Phys. B **18**, 4524 (2009)
- S.K. Kandpal, B. Goundie, J. Wright, R.A. Pollock, M.D. Mason, R.W. Meulenberg, A.C.S. Appl. Mater. Interfaces **3**, 3482 (2011)
- Z. Liu, Y. Li, Y. Xiong, D. Wang, Q. Yin, Microelectron. J. **35**, 375 (2004)
- D. Dutczak, C. Ronda, T. Jüstel, A. Meijerink, J. Phys. Chem. A **118**, 1617 (2014)
- P.A. Rodnyi, P. Dorenbos, G.B. Stryganyuk, A.S. Voloshinovskii, A.S. Potapov, C.W.E. van Eijk, J. Phys. Condens. Matter **15**, 719 (2003)
- S. Zhang, R. Pang, C. Li, Q. Su, J. Lumin. **130**, 2223 (2010)
- N.K. Zurba, I. Bdkin, A. Kholkin, D. Golberg, J.M.F. Ferreira, Nanotechnology **21**, 325707 (2010)
- S. Sakirzanovas, A. Katelnikovas, D. Dutczak, A. Kareiva, T. Jüstel, J. Lumin. **131**, 2255 (2011)
- B. Cheng, Z. Zhang, Z. Han, Y. Xiao, S. Lei, J. Mater. Res. **26**, 2311 (2011)
- Z. Liu, S. Chen, L. Meng, B. Liu, J. Mater. Sci. Mater. Electron. **26**, 6395 (2015)
- Y. Li, Y.H. Wang, Y. Xiong, T.Q. Peng, M.S. Mo, Appl. Mech. Mater. **152–154**, 198 (2012)
- T. Katsumata, Y. Kohno, H. Kubo, S. Komuro, T. Morikawa, Rev. Sci. Instrum. **76**, 084901 (2005)
- N. Suriyamurthy, B.S. Panigrahi, Inter. J. Lumin. Appl. **5**, 154 (2015)
- K. Song, J.-G. Mo, W. Chen, K. Feng, J. Mater. Sci. Mater. Electron. **27**, 49 (2016)
- F. Clabau, X. Rocquefelte, S. Jobic, P. Deniard, M.H. Whangbo, A. Garcia, T.L. Mercier, Solid State Sci. **9**, 608 (2007)
- A. Kumar, G. Kedawat, P. Kumar, J. Dwivedia, B.K. Gupta, New J. Chem. **39**, 3380 (2015)
- V. Singh, T.K.G. Rao, J.-J. Zhu, J. Solid State Chem. **179**, 2589 (2006)
- F.J. Baca, T.J. Haugan, P.N. Barnes, T.G. Holesinger, B. Maiorov, R. Lu, X. Wang, J.N. Reichart, J.Z. Wu, Adv. Funct. Mater. **23**, 4826 (2013)
- Y. Xin, Y. Qi, X. Ma, Z. Wang, Z. Zhang, S. Zhang, Mater. Lett. **64**, 2659 (2010)
- P. Ghosh, J. Oliva, E. De la Rosa, K.K. Haldar, D. Solis, A. Patra, J. Phys. Chem. C **112**, 9650 (2008)
- S. Mao, Q. Liu, M. Gu, D. Mao, C. Chang, J. Alloys Compd. **465**, 367 (2008)
- R. Punia, R.S. Kundu, J. Hooda, S. Dhankhar, S. Dahiya, N. Kishore, J. Appl. Phys. **110**, 033527 (2011)
- R.M. Oksuzoglu, P. Bilgic, M. Yildirim, O. Deniz, Opt. Laser Technol. **48**, 102 (2013)
- V.D. Mote, J.S. Dargad, B.N. Dole, Nanosci. Nanoeng. **1**, 116 (2013)
- A. Manikandan, J. Judith Vijaya, M. Sundararajan, C. Meganathan, L. John Kennedy, M. Bououdina, Superlatt. Microstruct. **64**, 118 (2013)
- V.R. Huse, V.D. Mote, B.N. Dole, World J. Condens. Matter Phys. **3**, 46 (2013)
- R. Viswanath, H.S.B. Naik, Y.K.G. Somalanaik, P.K.P. Neelan-jeneallu, K.N. Harish, M.C. Prabhakara, J. Nanotechnol. **2014**, 1 (2014)
- P. Herve, L.K.J. Vandamme, Infrared Phys. Technol. **35**, 609 (1994)
- C. Zhao, D. Chen, Y. Yuan, M. Wu, Mater. Sci. Eng. B **133**, 200 (2006)
- H. Sang-Do, K.C. Singh, T.-Y. Cho, H.-S. Lee, D. Jakhar, J.P. Hulme, C.-H. Han, J.-D. Kim, I.-S. Chun, J. Gwak, J. Lumin. **128**, 301 (2008)
- D.S. Kshatri, A. Khare, Opt. Spectrosc. **117**, 769 (2014)
- M. Peng, Z. Pei, G. Hong, Q. Su, Chem. Phys. Lett. **371**, 1 (2003)
- S.Y. Kaya, B. Karasu, G. Kaya, E. Karacaoglu, Adv. Sci. Technol. **62**, 88 (2010)
- F. Yu, Y. Yang, X. Su, C. Mi, H.J. Seo, Opt. Mater. Exp. **5**, 585 (2015)
- E.W. Barrera, C. Cascales, M.C. Pujol, K.H. Park, S.B. Choi, F. Rotermund, J.J. Carvajal, X. Mateos, M. Aguiló, F. Díaz, Phys. Procedia **8**, 142 (2010)
- T. Nakanishi, Y. Katayama, J. Ueda, T. Honma, S. Tanabe, T. Komatsu, J. Ceram. Soc. Jpn. **119**, 609 (2011)
- S.K.K. Shaat, H.C. Swart, O.M. Ntwaeaborwa, J. Alloys Compd. **587**, 600 (2014)

46. D.P. Bisena, R. Sharma, J. Biol. Chem. Lumin. (2015). doi:[10.1002/bio.2972](https://doi.org/10.1002/bio.2972)
47. P. Jander, W.S. Brocklesby, J. IEEE Quantum Electron. **40**, 509 (2004)
48. F.A. Abdel Wahab, M. Abdel-Baki, J. Non-Cryst. Solids **355**, 2239 (2009)
49. P. Kuruva, P.R. Matli, B. Mohammad, S. Reddigari, S. Katlakunta, J. Mag. Mater. **382**, 172 (2015)
50. M.M.S. Sanad, M.M. Rashad, E.A. Abdel-Aal, M.F. El-Shahat, K. Powers, J. Electon. Mater. **9**, 3559 (2014)
51. M.M.S. Sanad, M.M. Rashad, E.A. Abdel-Aal, M.F. El-Shahat, K. Powers, Mater. Chem. Phys. **162**, 299 (2015)
52. T. Shimada, K. Kura, S. Ohtsuki, J. Eur. Ceram. Soc. **26**, 2017 (2006)
53. H.-J. Kima, Y.K. Kimb, A. Jungc, S.-C. Choi, J. Ceram. Process. Res. **11**, 11 (2010)
54. L. Yi, L. Li, X.Q. Liu, X.M. Chen, J. Am. Ceram. Soc. **97**, 3531 (2014)